



Investigation of photosensitive properties of novel $\text{TiO}_2\text{:Cu}_2\text{O}$ mixed complex interlayered heterojunction: showcasing experimental and DFT calculations

Sinem Aksan¹ · Ali Akbar Hussaini^{2,3} · Mehmet Okan Erdal⁴ · Oğuzhan Taştan⁵ · Rabia Güzel⁵ · Şerife Saçmacı^{5,6} · Murat Yıldırım²

Received: 21 February 2023 / Accepted: 30 December 2023 / Published online: 30 January 2024
© The Author(s) 2024

Abstract

In this study, we investigated the effect of different reducing agents (ascorbic acid and sodium boron hydride) on optoelectronic properties of $\text{TiO}_2\text{:Cu}_2\text{O}$ nanocomposites. The $\text{TiO}_2\text{:Cu}_2\text{O}$ nanocomposites were characterized using X-ray diffractometry (XRD), Fourier transform infrared spectroscopy (FTIR), Field Emission Scanning Electron Microscopy (FESEM), and Energy dispersive X-ray (EDX). The electronic properties of the structure were calculated with the density functional theory (DFT). Both devices showed good responsivity and detectivity against light intensities. The photosensitivity of the devices had linear increasing profile with increasing light power. It is noteworthy that both devices demonstrated well-rectifying behaviors as a result of having low reverse bias and greater forward bias currents at the I - V characteristics in low light. The reduction of the band gap shifted the absorption band gap from the visible light region to the red edge. Density Functional Theory (DFT) calculations which has been done by using CASTEP are in good agreement with our experimental results. $\text{Ti}_{(1-x)}\text{Cu}_x\text{O}_2$ (7.5:1) band gap is 1.18 eV which is compared to the Shockley ve Quiser (SQ) limit. $\text{Ti}_{(1-x)}\text{Cu}_x\text{O}_2$ (15:1) band gap is 1.83 eV while the band gap is 2.28 eV for stoichiometric TiO_2 with our DFT calculations. Thus, the band gap narrowed with increasing Cu amount. This provides an improvement in light absorption. In conclusion, the results demonstrate that $\text{Al/TiO}_2\text{:Cu}_2\text{O/p-Si}$ can be used in optoelectronic applications.

Keywords Nanocomposite · Photodiode · $\text{TiO}_2\text{:Cu}_2\text{O}$ · Ultrasonic spray pyrolysis · DFT

1 Introduction

Despite the fact that modern semiconductor devices have only been around for 70 years, they have had a significant impact on human society (Al-Ahmadi 2020). The ohmic junction and the rectifying (also known as Schottky) junction are two perfect devices that come from close contact between a metal and a semiconductor (Di Bartolomeo 2016). Schottky heterojunctions function like a diode or rectifier, allowing carrier transmission at forward biases but prohibiting it at reverse biases (Demircioglu et al. 2011). They collect charge and energy in the interface when thought of as a capacitor. At reverse biases, they can also be used as a photodiode or photodetector (Yıldırım and Kocyigit 2018).

Extended author information available on the last page of the article

Metal–semiconductor heterojunctions have a wide range of applications such as photovoltaic cells, rectifiers, capacitors, photodiodes, photodetectors and transistors (Jin et al. 2015; Kocyigit et al. 2018; Könenkamp et al. 2005; Munikrishana Reddy et al. 2013; Orak et al. 2017; Yakuphanoglu 2007a; Yıldırım et al. 2022; Yücedağ et al. 2014). Among them, when compared to pn junction diodes, Schottky diodes offer a higher switching speed and temperature stability (Kyoung et al. 2016). Because Schottky diodes rely on majority carriers to operate (Anthopoulos et al. 2006).

Photodiodes are one of the most effective devices for converting light intensity into an electrical signal. The photodiode's characteristics determine how effectively the conversion process works. One of the most important advantages of photodiodes is that their quantum efficiency is independent of the junction distance. In this case, the wide-bandgap material acts as a transparent window for the incoming optical energy to pass through (Karataş et al. 2018; Mekki et al. 2016). When heterojunction structures are polarized in the opposite direction, their reverse current changes proportionally to the light falling on them. As is well known, when diodes are polarized in the opposite direction, reverse currents occur at the level of μA or nA . Therefore, photodiodes are made on the principle that reverse currents increase as the amount of light falling on them increases (Orak et al. 2017; Yilmaz et al. 2015). The active layer should be thin, often less than 100 nm, because of the poor mobility of charge carriers in these materials. Thinner layers allow better charge transmission, but they also lower the amount of light that is absorbed (Nyberg 2004).

The use of organics, metal oxides, and nanocrystals materials to improve the electrical properties of diodes is gaining popularity (Gullu et al. 2022; Karadeniz et al. 2022; Kocyigit et al. 2022a, c; Koçyiğit et al. 2021; Yathisha et al. 2019a, b; Yathisha and Nayaka 2020; Yıldırım et al. 2019). In electrical and optoelectronic applications, metal oxide semiconductors have received a lot of attention. The most versatile and well-known metal oxide compounds include titanium dioxide (TiO_2), copper(I) oxide (Cu_2O), cadmium oxide (CdO), nickel oxide (NiO), zinc oxide (ZnO), and tin oxide (SnO_2). Cu_2O has been utilized in application of solar cell (Wei et al. 2012; Zang 2018), photodetectors (Bai and Zhang 2016), diodes (Watahiki et al. 2017) and transistors (Yao et al. 2012). On the other hand, TiO_2 is another eminent metal oxide used in optoelectronic with a large bandgap of 3.2 eV (Dette et al. 2014). In the wavelength range of 300–1000 nm, the average transmittance of TiO_2 monolayer deposited on glass substrates was found higher than 95% (Shinen et al. 2018).

Within this study, we aimed to investigate the effects of different reducing agents on structure, morphology, and optoelectronic properties of the $\text{TiO}_2\text{:Cu}_2\text{O}$ nanocomposites. To the best of our knowledge, there is no study showing a minor change in synthesis of nanocomposites that could affect the efficiency of heterojunctions. On the scope this study, $\text{TiO}_2\text{:Cu}_2\text{O}$ complex is synthesized and utilized as interlayer in $\text{Al/TiO}_2\text{:Cu}_2\text{O}/p\text{-Si}$ heterostructure. $\text{TiO}_2\text{:Cu}_2\text{O}$ layer is investigated morphologically via FESEM, EDX, XRD, and FTIR. The electrical properties of $\text{TiO}_2\text{:Cu}_2\text{O}$ are investigated in detail via current-voltage and current-transient measurements via FY 7000 Solar Simulator.

2 Experimental

2.1 Material

All of the compounds used were of the analytical grade, and were employed without further purification. Titanium(IV) isopropoxide, ($\text{C}_{12}\text{H}_{28}\text{O}_4\text{Ti}$, purity 99% Fluka) was

used as a starting precursor for synthesizing crystalline TiO_2 particles. Copper nitrate as a dopant precursor, propan-2-ol, ethanol, acetic acid, ascorbic acid, and sodium dodecyl sulfate (SDS) were purchased from Merck (Germany). Ultra-pure water with a resistivity of $18.2 \text{ M}\Omega \text{ cm}$ was obtained from a Milli-Q system (Millipore, USA). Hydrofluoric acid (HF, 48%), isopropyl alcohol ($(\text{CH}_3)_2\text{CHOH}$, $\geq 99.7\%$), and acetone (CH_3COCH_3 , $\geq 99.5\%$) were obtained from Merck. Boron doped Si with (111) orientation, $1\text{--}20 \text{ }\Omega \text{ cm}$ resistivity and $500\text{--}550 \text{ }\mu\text{m}$ thickness was purchased from Wafer World. 99.99% aluminum (Al) was purchased from Sigma-Aldrich to obtain ohmic and metallic contacts.

2.2 The synthesis of $\text{TiO}_2\text{:Cu}_2\text{O}$ complexes

Synthesis of $\text{TiO}_2\text{:Cu}_2\text{O}$ oxide complexes was carried out by hydrothermal method. In the initial step, 24 mL of the solvent (propan-2-ol) and the required quantity of titanium(IV) isopropoxide were added to a reactor using a Daihan-MSH-20D high-speed stirrer. Using a burette, 0.1% copper nitrate aqueous solution was continuously added to this mixture. At room temperature and 500 rpm, the mixture was stirred. To achieve pH 4.5, 3 mL of a 0.2 mol/L acetic acid solution was then gradually added to the mixture. As reductant agents, 0.1 mL of 0.1 mol/L ascorbic acid and sodium boron hydride were used and mixed with 1 mL of 0.1 mol/L sodium dodecyl sulfate separately. After that, the resulting mixture was added to the suspension. Resulting solution was stirred at room temperature for 60 min. After which it was placed in an oven and hydrothermally treated for 12 h at $180 \text{ }^\circ\text{C}$. The materials collected from the hydrothermal reactor were filtered and washed three times with deionized water before being cooled at ambient temperature. The resulting $\text{TiO}_2\text{:Cu}_2\text{O}$ oxide complexes were dried at $60 \text{ }^\circ\text{C}$ for 6 h. $\text{TiO}_2\text{:Cu}_2\text{O}$ complexes synthesized via ascorbic acid and sodium boron hydride reducing agents were labeled as M1 and M2, respectively.

2.3 Fabrication

$\text{TiO}_2\text{:Cu}_2\text{O}$ nanocomposite synthesized via ascorbic acid as reducing agent (M1) and $\text{TiO}_2\text{:Cu}_2\text{O}$ nanocomposites synthesized via sodium boron hydride as reducing agent (M2) were used as interlayers to fabricate Al/M1/*p*-Si (D1) and Al/M2/*p*-Si (D2) photodiode device, respectively. Si wafers were cut into 15 mm^2 pieces after being cleaned using the RCA cleaning technique (Kern and Puotinen 1970). To remove the contaminants, *p*-type Si pieces were subjected to an $\text{HF:H}_2\text{O}$ (1:10) treatment. They were then transported to a thermal evaporator to make ohmic contacts after cleaning. At 6×10^{-6} Torr, a 100 nm Al layer was deposited on the back of Si wafers. They were then subjected to a $500 \text{ }^\circ\text{C}$ temperature for five minutes in a N_2 environment. $\text{TiO}_2\text{:Cu}_2\text{O}$ nanocomposites were added to distilled water (5 g/L concentration), then put onto magnetic stirrer for 1 h. $\text{TiO}_2\text{:Cu}_2\text{O}$ solution was deposited on the front surface of the wafer via ultrasonic spray pyrolysis (USP). 5 mL of the $\text{TiO}_2\text{:Cu}_2\text{O}$ solution was placed in ultrasonic nebulizer vibrated at a frequency of 50 kHz. With 3 cm spacing between the plate and the nozzle and a 25 mL/h spray rate, USP was carried out as the nozzle moved on a hot plate that had been annealed at $200 \text{ }^\circ\text{C}$. Al was evaporated onto the $\text{TiO}_2\text{:Cu}_2\text{O}$ surface using a 1 mm hole array mask to produce metallic contact at 5×10^{-6} Torr. Figure 1 displays a schematic representation of the fabricated heterojunction.

Fig. 1 Schematic structure of the device

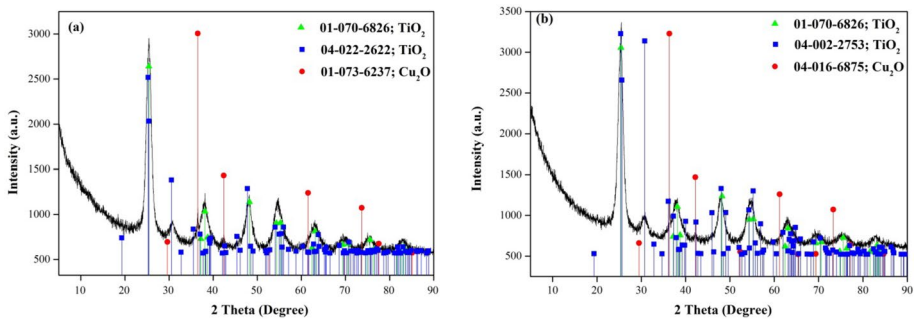
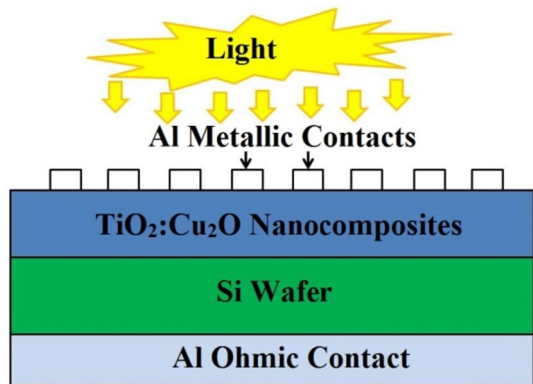


Fig. 2 XRD pattern of **a** M1 and **b** M2

3 Results and discussion

3.1 Morphological analysis

Particularly for crystalline materials, X-ray diffraction (XRD) is a trusted and common identification method (Barakat et al. 2013). Using the XRD, the crystal characteristics of the produced binary oxide systems were investigated. It was performed at 40 kV and 40 mA with a 0.02° step angle in the $2\theta = 10^\circ\text{--}90^\circ$. DiffracPlus and Win-Metric applications were used to index the XRD powder pattern; and to determine the unit cell parameters.

As can be seen from Fig. 2, the samples show peaks corresponding to the tetragonal and orthorhombic phases at two values of green and blue peaks respectively. Additionally, the sample peak (01-073-6237, red peak) is Cu_2O . This is attributed to reactions of tetragonal and orthorhombic TiO_2 which is compared with JCPDS Card No. (21-1272). (101), (110), (111), (200), (115), (213), (220), (222), and (224) planes were observed at $2\theta = 25.4^\circ$, 30.6° , 37.7° , 47.9° , 54.6° , 63.0° , 69.6° , 75.2° , and 82.9° , respectively.

Parameters such as crystallite size (D), microstrain (ϵ), texture coefficient and dislocation density (ρ) can be calculated as described in (Yathisha et al. 2016; Yathisha and Arthoba Nayaka 2018). Sharp diffraction peaks indicate the crystallinity of the materials, whereas irregular or curved surfaces indicate amorphous structure. The texture coefficients

of the synthesized $\text{TiO}_2\text{:Cu}_2\text{O}$ films provide a numerical description of the texture of the planes. The values of the planes' ($\text{TC}_{(hkl)}$) coefficients are given by the following relation:

$$\text{TC}_{(hkl)} = \frac{I_{(hkl)}/I_{0(hkl)}}{N^{-1} \sum_N I_{(hkl)}/I_{0(hkl)}} \quad (1)$$

$I_{(hkl)}$ stands for the peak intensities, $I_{0(hkl)}$ is the standard reference intensity value for the (hkl) planes, and the number of diffraction lines overall is N . To investigate the influence of the microstructural characteristics, parameters such as the crystallite size (D), micro-strain (ε), and dislocation density (ρ) were calculated from XRD graphs using the following equations:

$$D = \frac{0.94\lambda}{\beta \cos\theta} \quad (2)$$

$$\varepsilon = \frac{\beta \cos\theta}{4} \quad (3)$$

$$\rho = \frac{15\varepsilon}{\alpha D} \quad (4)$$

θ , β , and λ stand for the Bragg's diffraction angle, the peak's FWHM value, and the X-ray wavelength, respectively. Considering the lattice constant of TiO_2 as 4.84 Å and Cu_2O as 4.26 Å (Wisiz et al. 2023), parameters of D , ε and ρ values were calculated for (101), (110), (111), (200), (115), (213), (220), (222), and (224) planes, as shown in Table 1. M1 and M2 indicate mean crystallite sizes of 4.70 nm and 4.57 nm, respectively. Mean micro-strain values for M1 and M2 were calculated as 8.782×10^{-3} and 8.363×10^{-3} , respectively. Mean dislocation density values for M1 and M2 were calculated as $8.188 \times 10^7 \text{ cm}^{-2}$ and $6.719 \times 10^7 \text{ cm}^{-2}$, respectively.

The surface morphology of $\text{TiO}_2\text{:Cu}_2\text{O}$ binary oxide system was investigated by FESEM (Zeiss Gemini 500) with EDX to carry out the characterization studies of the materials prepared in the present study.

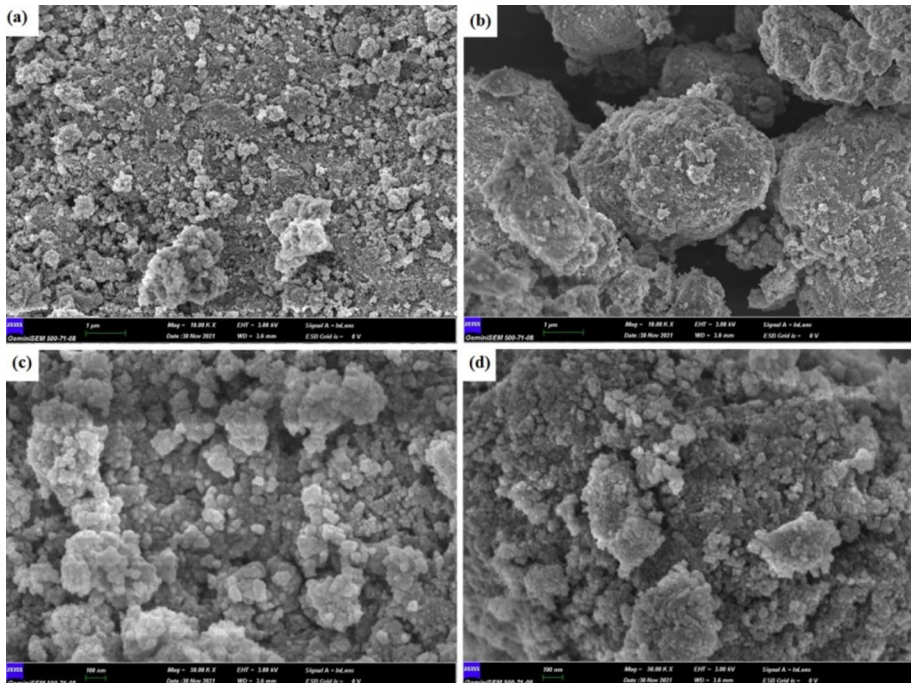
FESEM images of $\text{TiO}_2\text{:Cu}_2\text{O}$ microspheres synthesized at pH ~4.5, for 12 h at 180 °C is shown in Fig. 3. The surface of the chemically synthesized $\text{TiO}_2\text{:Cu}_2\text{O}$ powder was composed of small particles, as seen in the FESEM images. At 180 °C, the nanoparticles were compacted together, making it challenging to measure the size of each particle. Although all of the FESEM images of the compositions are identical to one another, their sizes vary. Therefore, the hydrothermal method creates stable gels that result in smaller nanoparticles. They are observed to be in a moderate aggregation state. The particles are finer but their edges were not sharp, and their distributions were homogeneous when FESEM images were examined. Using measurements taken while varying the temperature and pH parameters, the optimal experimental conditions were found as a consequence of all optimization studies. The ideal calcination temperature is 180 °C for 12 h, and the ideal pH is 4.5.

Particle measurements were calculated by ImageJ program, shown in Fig. 4. M1 has average particle size of 38 nm, whereas M2 particles were smaller compared to M1 with an average particle size of 29 nm.

Additionally, EDX was used to identify the components of the composite materials, as shown in Fig. 5. The synthesized materials are compatible with the synthesized stoichiometry, according to the EDX studies.

Table 1 Parameters extracted from XRD graphs

Nanocomposite	Planes	Peak intensity	TC _(hkl)	Crystallite size (nm)	Microstrain (ϵ) $\times 10^{-3}$	Dislocation density ($10^7 \times \text{cm}^{-2}$)
M1	(101)	2934	2.52	7.39	4.89	2.21
	(110)	903	0.77	2.22	16.3	24.47
	(111)	1126	0.97	2.86	12.66	14.76
	(200)	1191	1.02	4.76	7.6	5.32
	(115)	1184	1.02	3.97	9.13	7.67
	(213)	903	0.77	4.10	8.83	7.18
	(220)	773	0.66	4.75	7.62	5.35
	(222)	751	0.64	5.39	6.72	4.15
	(224)	730	0.63	6.84	5.29	2.57
M2	(101)	3323	2.67	7.69	4.70	2.04
	(110)	1020	0.82	3.34	10.82	10.78
	(111)	1180	0.95	3.47	10.44	10.04
	(200)	1238	0.99	4.93	7.34	4.96
	(115)	1204	0.97	5.07	7.14	4.70
	(213)	952	0.76	4.21	8.60	6.82
	(220)	792	0.63	3.97	9.12	7.66
	(222)	768	0.61	4.13	8.76	7.07
	(224)	742	0.59	4.35	8.31	6.37

**Fig. 3.** 10,000 \times magnified images of **a** M1 and **b** M2 nanocomposites, 50,000 \times magnified images of **c** M1 and **d** M2 nanocomposites

The $\text{TiO}_2:\text{Cu}_2\text{O}$ microsphere created using the hydrothermal method's FTIR spectrum is shown in Fig. 6 and its spectrum displays a number of distinctive peaks. The stress in the metal oxide's vibration mode ($\text{M}-\text{O}$) may be responsible for the peaks in the range of $47\text{--}458\text{ cm}^{-1}$. The XRD evidence that supports the formation of the metal oxides Ti and Cu:Ti is supported by the stretching vibration mode of the metal oxide.

3.2 Electrical properties

Electrical characteristics of the $\text{TiO}_2:\text{Cu}_2\text{O}$ interlayered photodiode was obtained by $I-V$ measurements. Figure 7a and b show the $\ln I - V$ characteristics of the D1 and D2 photodiodes under 0, 20, 40, 60, 80, and 100 mW/cm^2 illumination intensities. Given that light causes the current to increase at both zero and the reverse bias voltage, the constructed heterostructures exhibit excellent photodiode behavior.

Rectifying ratio (RR) plots of the D1 and D2 photodiodes has been calculated using $RR = I_{\text{forward}}/I_{\text{reverse}}$ formula at $\pm 3\text{ V}$, and illustrated in Fig. 8. The highest RR value was obtained under dark condition. It had good rectifying qualities because in the dark, it had a higher forward bias current and a lower reverse bias current. Generally, the RR values of the devices were decreased by increasing illumination. The D1 Photodiode has higher RR profile compared to D2 device.

Several methods, including thermionic emission, Norde and Cheung approximations, can be used to determine the photodiode parameters. The values for the ideality factor (n), series resistance (R_s), and barrier height (Φ_B) were computed using the methods indicated above and are shown in Table 2. According to the thermionic emission theory, $V > 3kT$ is assumed and the following equations can be used (Yildirim 2017):

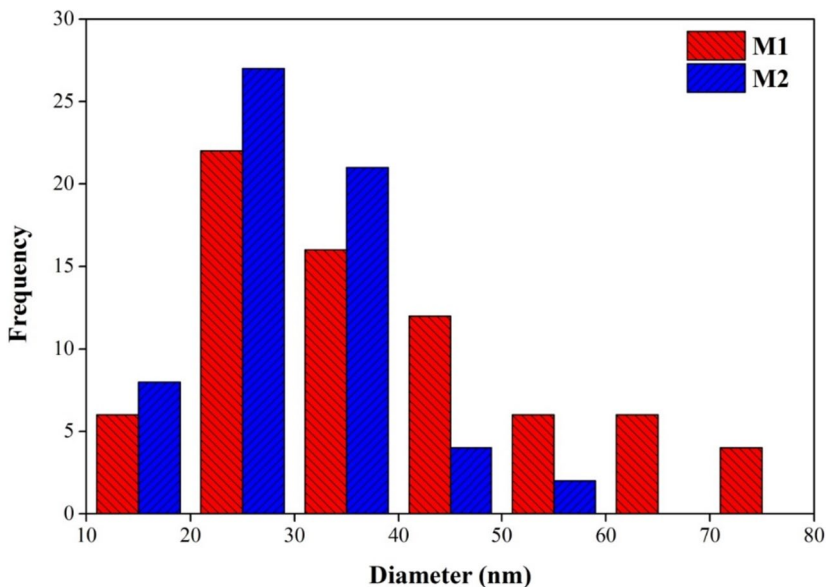


Fig. 4 Diameter calculation of M1 and M2 nanocomposites

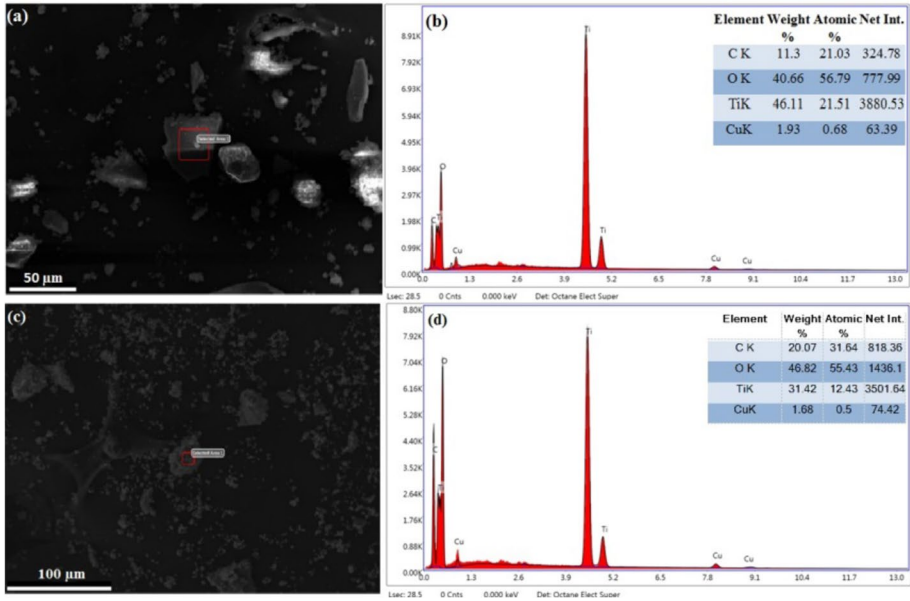


Fig. 5 EDX pattern of a, b M1, and c, d M2

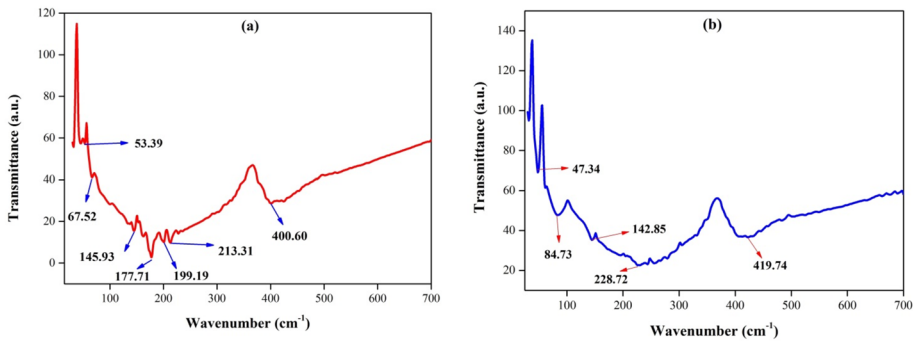


Fig. 6 FTIR graphic of a M1 and b M2

$$I = I_0 \left[\exp\left(\frac{qV}{nkT}\right) - 1 \right]; \tag{5}$$

$$I_0 = AA^*T^2 \exp\left(-\frac{q\Phi_B}{kT}\right)$$

here, I_0 stands for saturation current, n is ideality factor, q is electronic charge, A is contact area used in measurements, A^* is Richardson constant (for p type silicon, $A^* = 32 \text{ A/cm}^2 \text{ K}^2$), Φ_B barrier height and T is the absolute temperature. The n and Φ_B are calculated via the following equations for $V > 3kT/q$.

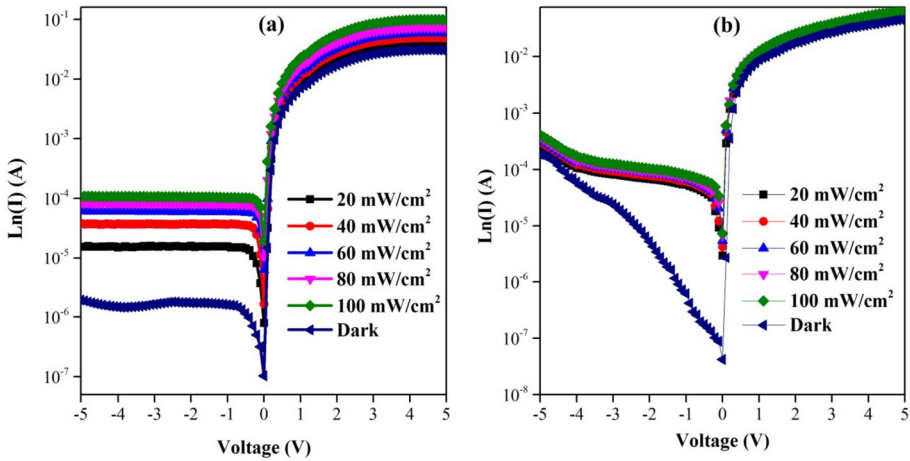


Fig. 7 $\ln I - V$ graphics a D1 and b D2 photodiodes

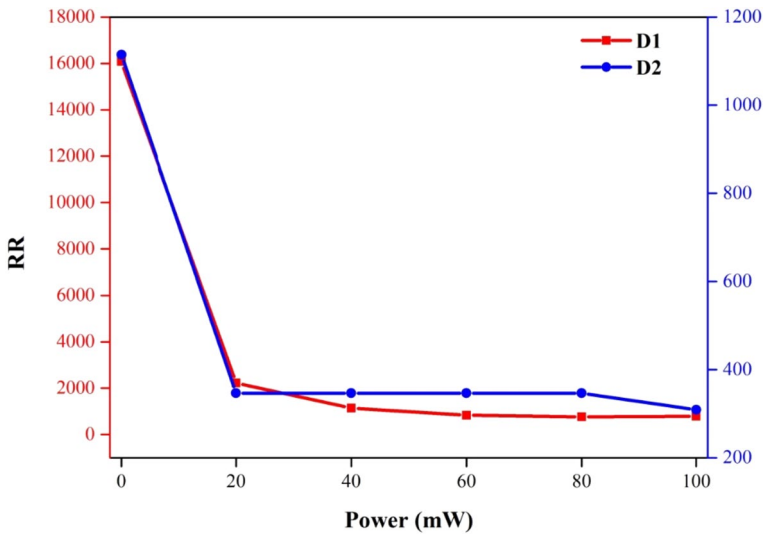


Fig. 8 RR plots of the D1 and D2 devices

$$\Phi_B = \frac{kT}{q} \ln \left(\frac{AA^*T^2}{I_0} \right) \quad \text{and} \quad n = \frac{q}{kT} \frac{dV}{d \ln(I)} \quad (6)$$

Saturation currents of M1 and M2 interlayered devices were increased to 5.40×10^{-5} A and 1.78×10^{-5} under 100 mW/cm^2 . Ideality factor was calculated as 2.33 and 1.47 under 100 mW/cm^2 for the M1 and M2 interlayered devices, respectively. Barrier height were calculated according to I_0 values and were found as 0.514 eV and 0.542 eV under 100 mW/cm^2 for M1 and M2 interlayered devices, respectively. Ideality factor and barrier height of the both devices were calculated under 0, 20, 40, 60, 80 and 100 mW/cm^2 illumination,

Table 2 Diode parameters obtained by TE, Cheung, and Norde's approaches

Device	Saturation Current (I_0)	$n (I-V)$	n Cheung –	$\Phi_b (I-V)$ (eV)	Φ_b Cheung (eV)	Φ_b Norde (eV)	R_s Cheung ($k\Omega (H(f))$)	R_s Cheung ($k\Omega (d\ln(I))$)	R_s Norde ($k\Omega$)
Al/M1/p-Si	5.40×10^{-5}	2.33	2.36	0.514	0.505	0.507	0.024	0.034	0.042
Al/M2/p-Si	1.78×10^{-5}	1.47	1.47	0.542	0.504	0.524	0.054	0.079	0.023

shown in Fig. 9a and b. As seen in Fig. 9b, the increase in charge carriers with illumination is what causes the drop in barrier height values with an increase in light intensity (Li et al. 2017). For all devices, the ideality factor values increased as the light power intensity increased due to an increase in forward bias current velocity (Kocytigit et al. 2022b).

According to Cheung's approach, the current is given by the following equation:

$$I = I_0 \exp\left(-\frac{q(V - IR_s)}{nkT}\right) \quad (7)$$

where IR_s is the voltage difference falling across the series resistance. The following relations can be obtained for the Cheung approximation:

$$\frac{dV}{d(\ln I)} = IR_s + n \frac{kT}{q} \quad (8)$$

$$H(I) = V - n \left(\frac{kT}{q}\right) \ln\left(\frac{I}{AA^*T^2}\right) \quad (9)$$

where $H(I)$ is rearranged:

$$H(I) = IR_s + n\Phi_B \quad (10)$$

The functions listed above result in a linear variation in current when Eqs. (8) and (9) are plotted versus current. The values where this graph cuts the slope and the y-axis, respectively, can be used to determine R_s and $n \frac{kT}{q}$ if the $dV/(d(\ln I)) - I$ change is plotted. Φ_B and R_s value can be calculated using these values. However, if a graph of $H(I)$ versus I is drawn, R_s and $n\Phi_B$ values can be calculated from the point where this graph cuts the slope and y-axis, respectively (Cheung and Cheung 1986). The Cheung plots of the D1 and D2 devices were shown in Fig. 10a and b, respectively. Calculated n and Φ_B are in good agreement with the outcomes of the thermionic emission theory, according to Table 1. Additionally, the device's R_s values as determined by $dV/(d(\ln I)) - I$ and $H(I) - I$ graphics are in good accord with one another and support the validity of Cheung technique.

Additionally, Norde's technique can be used to calculate the barrier height and series resistance. The parameters provided by the Norde's technique are presented in the following equations (Norde 1979):

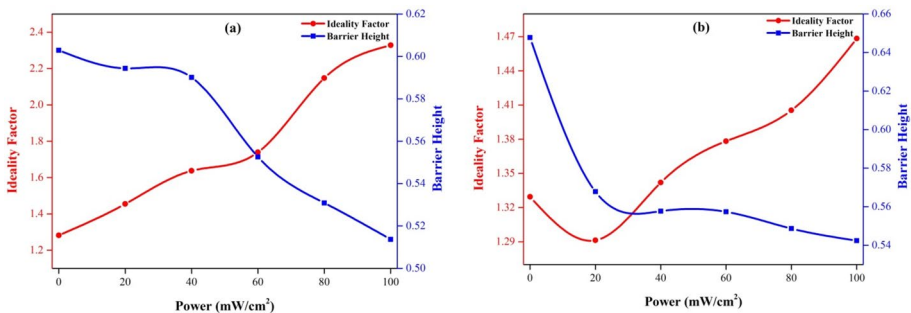


Fig. 9 $n\Phi_B$ plots of the a D1 and b D2 devices

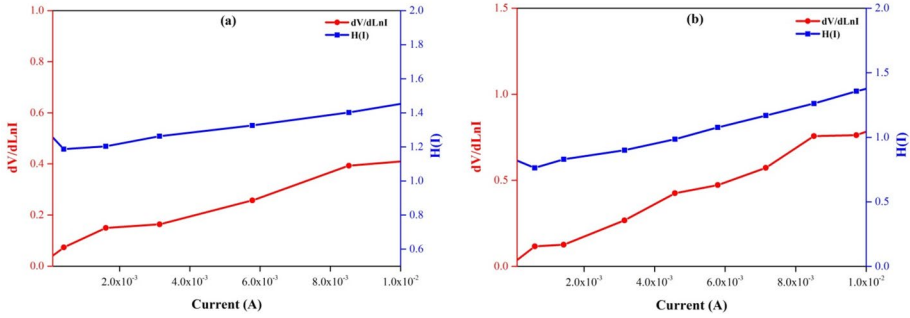


Fig. 10 Cheung plots of the a D1 and b D2 devices

$$F(V) = \frac{V}{\gamma} - \frac{kT}{q} \ln \frac{I(V)}{AA^*T^2} \tag{11}$$

The closest integer higher than the ideality factor is γ , and $I(V)$ is the voltage-dependent current that is expressed. The following equations are used to determine Φ_B and R_s :

$$\Phi_B = F(V_0) + \left[\frac{V_0}{\gamma} - \frac{kT}{q} \right] \tag{12}$$

and,

$$R_s = \frac{\gamma - n}{I} \frac{kT}{q} \tag{13}$$

here V_0 is the minimum voltage in the $F(V)$ graphics. Figure 11 shows the $F(V)$ versus V plots of the the photodiodes. The calculated Φ_B and R_s values are given in Table 1 for both devices. The γ values were determined as 3 and 2 for D1 and D2 devices at 100 mW/cm², respectively. V_0 was found as 0.505 and 0.500 for D1 and D2 at 100 mW/cm², respectively. The obtained Φ_B and R_s values agree well with other approximations. The Φ_B and R_s values may differ slightly due to approximation (Yilmaz et al. 2020).

The device’s optical detector parameters are determined by its current transient properties. $I-t$ plots can be used to determine the device’s photocurrent (I_p), photosensitivity (K), responsivity (R), and specific detectivity (D^*). $I-t$ plots of the D1 and D2 devices have been shown in Fig. 12a and b. For every light power illumination, the devices were seen to respond instantly. The current amount increased with the TiO₂:Cu₂O complexes addition. With illumination, these values clearly increase in Fig. 12, and when illumination is inhibited, the trend is reversed. The production of free charge carriers is sparked by illumination, which then increases current flow. With a rise in the quantity of charge carriers, the photocurrent reaches its saturation threshold under these circumstances. These carriers are held at lower levels when the light is turned off, and the initial level of current is seen in roughly a second (Gullu et al. 2022; Yakuphanoglu 2007b).

The following equations, respectively, are used to formulate the values for photocurrent (I_p), photosensitivity (K), responsivity (R), and specific detectivity (D^*).

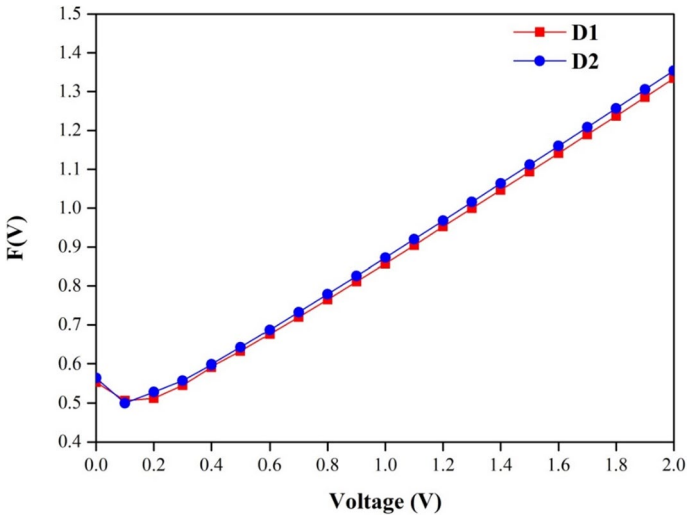


Fig. 11 $F(V)$ graphics of a D1 and b D2 devices

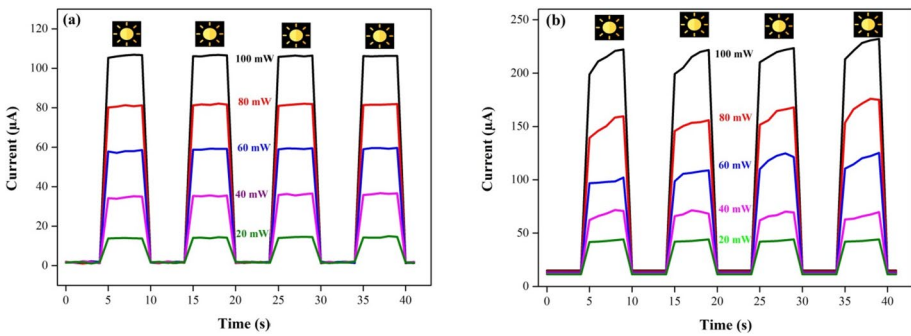


Fig. 12 $I-t$ plots of the a D1 and b D2 devices

$$I_p = I_{light} - I_{dark} \tag{14}$$

$$K = \frac{I_p}{I_{dark}} \tag{15}$$

$$R = \frac{I_p}{P_A} \tag{16}$$

$$D^* = R \sqrt{\frac{A}{2qI_{dark}}} \tag{17}$$

A stands for the effective detector area, and P for incident power density. The three crucial criteria for photodiode or photodetector applications are responsiveness, photosensitivity, and specific detectivity. Specific detectivity is the detection of a weak signal, photosensitivity is the degree of incident light detection, and responsiveness is the response of incident light (Dayan et al. 2020; Yenel et al. 2021). Photosensitivity, responsiveness, and specific detectivity of the heterostructures were listed in Table 3. Increasing light intensity causes an increase in values at constant $\text{TiO}_2\text{:Cu}_2\text{O}$ concentrations, which is connected to an increase in the diode's photo-sensitivity properties.

Photosensitivity of the D1 and D2 devices are shown in Fig. 13. While the D2 device nearly exhibits linear change as light power increases, the D1 device exhibits some deviation from linearity at illumination intensities of 100 mW/cm^2 . Moreover, both devices exhibit a rather high photoresponsivity.

The responsivity of the D1 and D2 devices are shown in Fig. 14. The devices showed strong responsivity values. Responsiveness of both devices increased as light power intensity increased.

Specific detectivity profiles of the D1 and D2 devices, respectively, for varying light power intensity, are shown in Fig. 15. The D^* values of the D1 device increased as the light power intensity approached 80 mW/cm^2 , and they subsequently started to decline at 100 mW/cm^2 light power intensity. In other device, it decreased at 40 and 60 mW/cm^2 and increased toward 100 mW/cm^2 .

4 DFT calculations

Calculations based on Density Functional Theory with molecular modeling method were performed to solve Kohn–Sham equations using projective combined wave (PAW) potential (Hohenberg and Kohn 1964). Energy calculations were obtained using the CASTEP simulation module by Materials Studio. Electronic exchange and correlation effects are taken into account with the Generalized Gradient Approach (GGA) developed by Perdew, Burke and Ernzerhof (PBE) (Perdew et al. 1996). In this study, Cu^{+1} ion was added instead of Ti^{+4} ions in TiO_2 Anatase crystal form. The electronic and structural properties of the

Table 3 Photodetector parameters under various illumination intensities

Devices	Power (mW/ cm^2)	Photocurrent (A)	Photosensitivity –	Responsivity (A/W)	Specific detectivity (Jones)
Al/M1/p-Si	20	1.22×10^{-5}	6.92	0.078	9.16×10^9
	40	3.24×10^{-5}	14.69	0.103	1.09×10^{10}
	60	5.63×10^{-5}	32.65	0.120	1.43×10^{10}
	80	8.02×10^{-5}	75.60	0.128	1.94×10^{10}
	100	1.05×10^{-4}	75.48	0.134	1.78×10^{10}
Al/M2/p-Si	20	3.28×10^{-5}	2.89	0.209	9.70×10^9
	40	5.87×10^{-5}	4.83	0.187	8.40×10^9
	60	8.92×10^{-5}	6.91	0.189	8.25×10^9
	80	1.46×10^{-4}	10.47	0.232	9.73×10^9
	100	2.07×10^{-4}	13.90	0.264	1.07×10^{10}

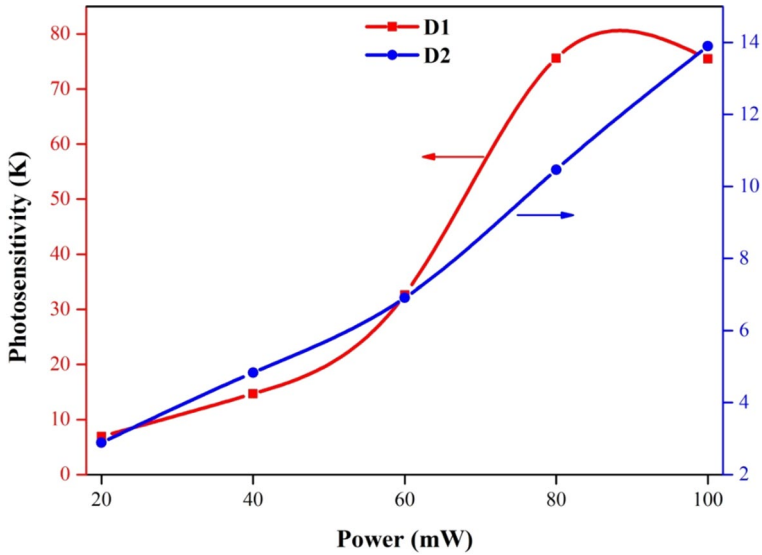


Fig. 13 Photosensitivity of the a D1 and b D2 devices

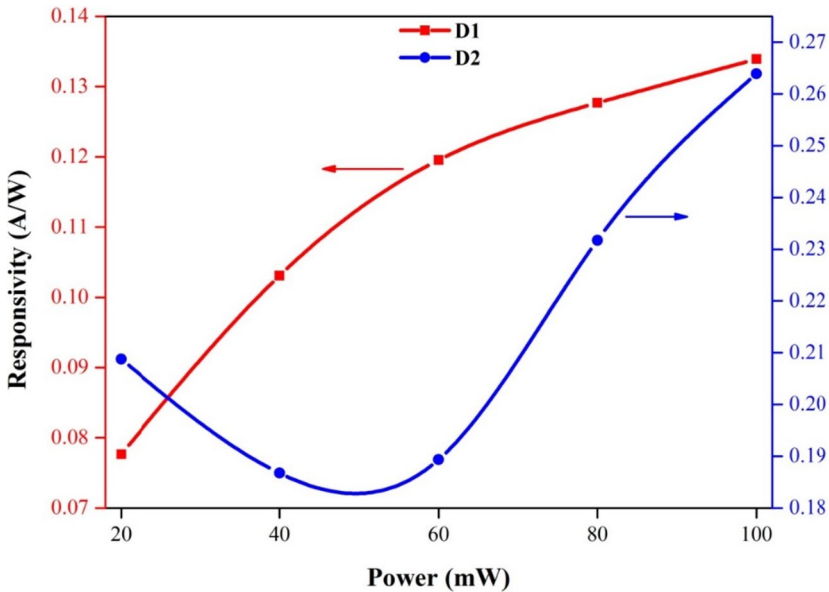


Fig. 14 Responsivity profile of the a D1 and b D2 devices

stoichiometric TiO_2 and non-stoichiometric $\text{Ti}_{1-x}\text{Cu}_x\text{O}$ crystal forms obtained in this way and investigated as $2 \times 1 \times 1$ super cell (Fig. 16). Kinetic energy cut-off values for all crystal forms were determined as 800 eV. It is used to get the integration of the Brillouin zone in inverse space.

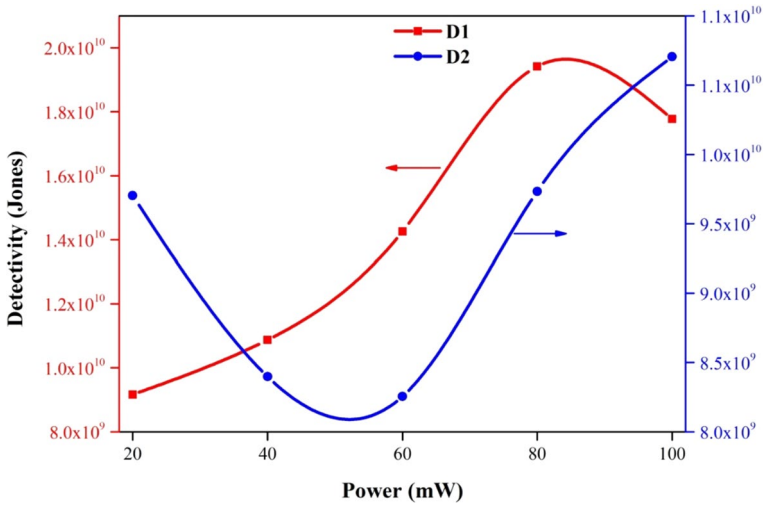


Fig. 15 Specific detectivity profile of the **a** D1 and **b** D2 devices

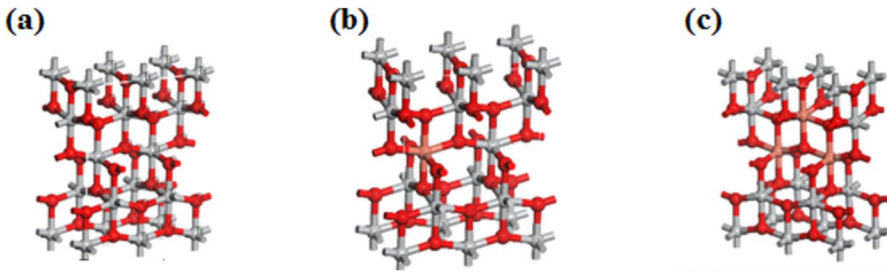


Fig. 16 Stoichiometric TiO_2 and Non-stoichiometric $\text{Ti}_{1-x}\text{Cu}_x\text{O}$ crystal forms ($2 \times 1 \times 1$) Red atoms: O ●, Gray Atoms: Ti ● and Orange Atoms: Cu ● for Stoichiometric TiO_2 Super Cell, **b** $\text{Ti}_{1-x}\text{Cu}_x\text{O}$ (15:1) Super cell, and **c** $\text{Ti}_{1-x}\text{Cu}_x\text{O}$ (7.5:1) Super cell

In the calculations, in order to calculate the lattice constants in the equilibrium state of the crystal phases and the structure with the smallest energy, the atoms dispersed according to crystal symmetry. It could be separated from their positions in three directions, the force and stress applied to them, the volume and shape of the unit cell could be changed, and the outer layer was applied on the crystal system is allowed. By iterating the pressure to approximately 0 kbar and the total force applied on each atom to $\sim 0.01 \text{ eV/\AA}$ per length, the crystal structure with the lowest energy was obtained. In the Fig. 17, it is seen that the energy is minimized with the energy optimization steps graph.

The modelling structure of TiO_2 had been chosen according to our XRD results which is compared with JCPDS Card No. (21-1272). The lattice parameters are according to JCPDS card $a=3.7852$ $b=3.7852$ $c=9.5139$. Stoichiometric TiO_2 's lattice parameters were calculated after copper addition and geometric optimization of super cell ($2 \times 1 \times 1$) and the lattice parameters are $a=7.300444$ $b=3.778885$ $c=9.992898$ and cell angles; $\alpha = \beta = \gamma = 90$ and non-stoichiometric $\text{Ti}_{(1-x)}\text{Cu}_x\text{O}_2$ (15:1) $a=7.552000$ $b=3.776000$ $c=9.486000$ and non-stoichiometric $\text{Ti}_{(1-x)}\text{Cu}_x\text{O}_2$ (7.5:1)

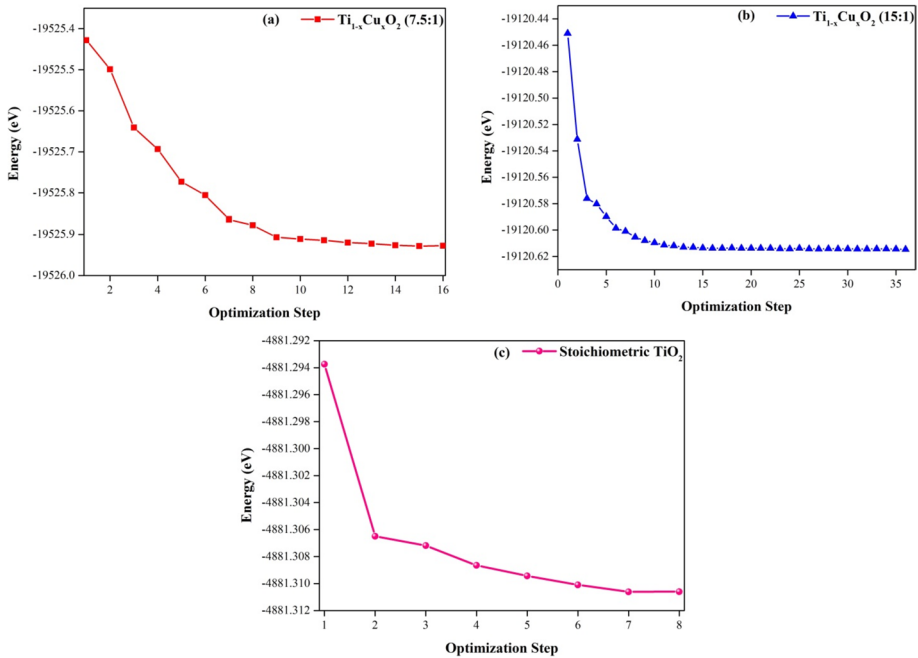
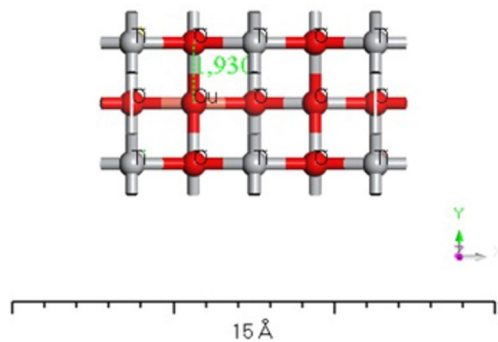


Fig. 17 Geometric Optimization of the Crystal System of **a** $\text{Ti}_{1-x}\text{Cu}_x\text{O}_2$ (7.5:1), **b** $\text{Ti}_{1-x}\text{Cu}_x\text{O}_2$ (15:1) and, **c** Stoichiometric TiO_2

$a = 7.300444$ $b = 3.778885$ $c = 9.992898$. Ti–O bond length is 1.930 \AA . The bond length for $\text{Ti}_{(1-x)}\text{Cu}_x\text{O}_2$ (7.5:1) is Ti–O 1.965 \AA ; Cu–O is 2.026 \AA (Fig. 18) and it is in line with the literature (Jiang et al. 2021). The bond length increased with the addition of copper oxide. Also our supercell parameters which are anatase form match very closely with our experimental XRD results that have been shown in Fig. 2.

Electronic properties of $\text{Ti}_{(1-x)}\text{Cu}_x\text{O}_2$ (15:1) structure are examined from the pDOS graphs given in Fig. 19. The lowest valence bands around -5 eV are predominantly due to the $3s$, $3p$ and $3d$, $4s$ states of Ti atoms. The Fermi level and the valence band around -3 eV are predominantly composed of the s and p states of O atoms. The s , p and d

Fig. 18 Bond lengths of $\text{Ti}_{(1-x)}\text{Cu}_x\text{O}_2$



states of Ti atoms are dominant in the contributions to the conduction band, which is distributed between 2 and 6 eV, especially in the lower parts of the band. At 3 eV and above, contributions from both Ti and O and above 6 eV contributions from Cu atoms are observed.

Contributions from Cu atoms come from the $3d^{10} 4s^1$ states. The band gap for TiO_2 is 2.20 eV with DFT calculations. The band gap of $\text{Ti}_{(1-x)}\text{Cu}_x\text{O}_2$ (7.5:1) is 1.18 eV which is at the top of the valence band and at the bottom of the conduction band. This value is compared to the SQ limit. $\text{Ti}_{(1-x)}\text{Cu}_x\text{O}_2$ (15:1) band gap is 1.83 eV as it can be seen from Fig. 19. The band gap is 2.28 eV for stoichiometric TiO_2 with our DFT calculations (Fig. 20). The band gap narrowed with increasing copper addition. This depends on the electron state density. Our DFT calculations are in agreement with our experimental results. The reduction of the band gap shifted the absorption band gap from the visible light region to the red edge. This provides an improvement in light absorption.

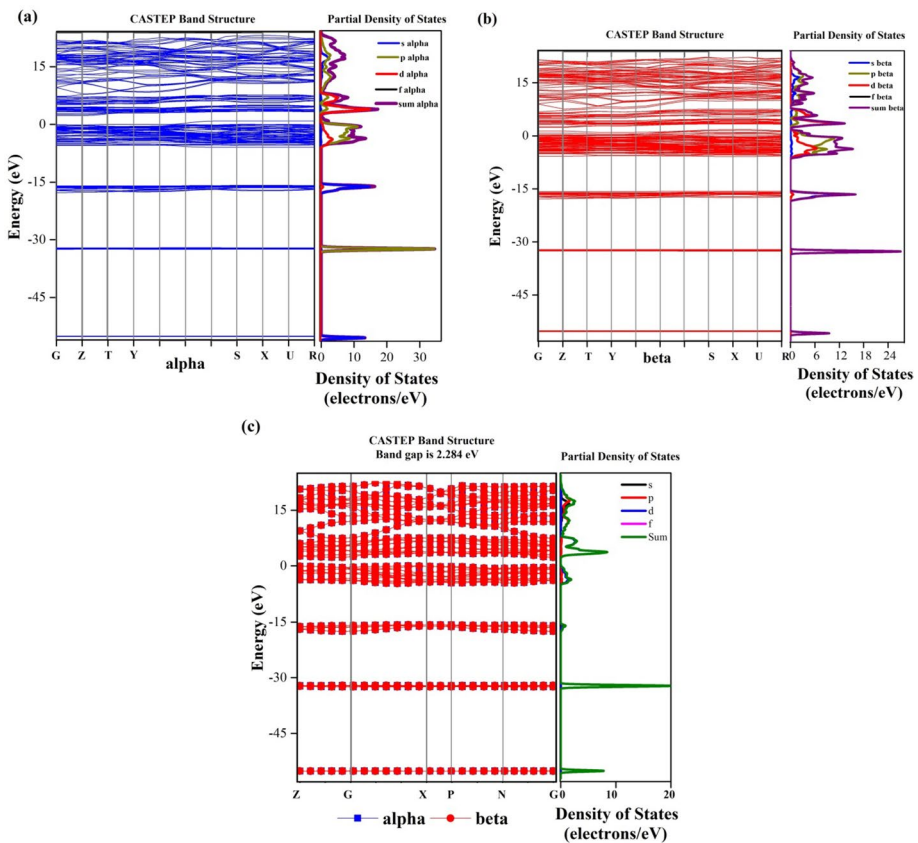


Fig. 19 The band gap and PDOS graphics of the **a** $\text{Ti}_{1-x}\text{Cu}_x\text{O}_2$ (15:1), **b** $\text{Ti}_{1-x}\text{Cu}_x\text{O}_2$ (7.5:1) and, **c** stoichiometric TiO_2 PDOS

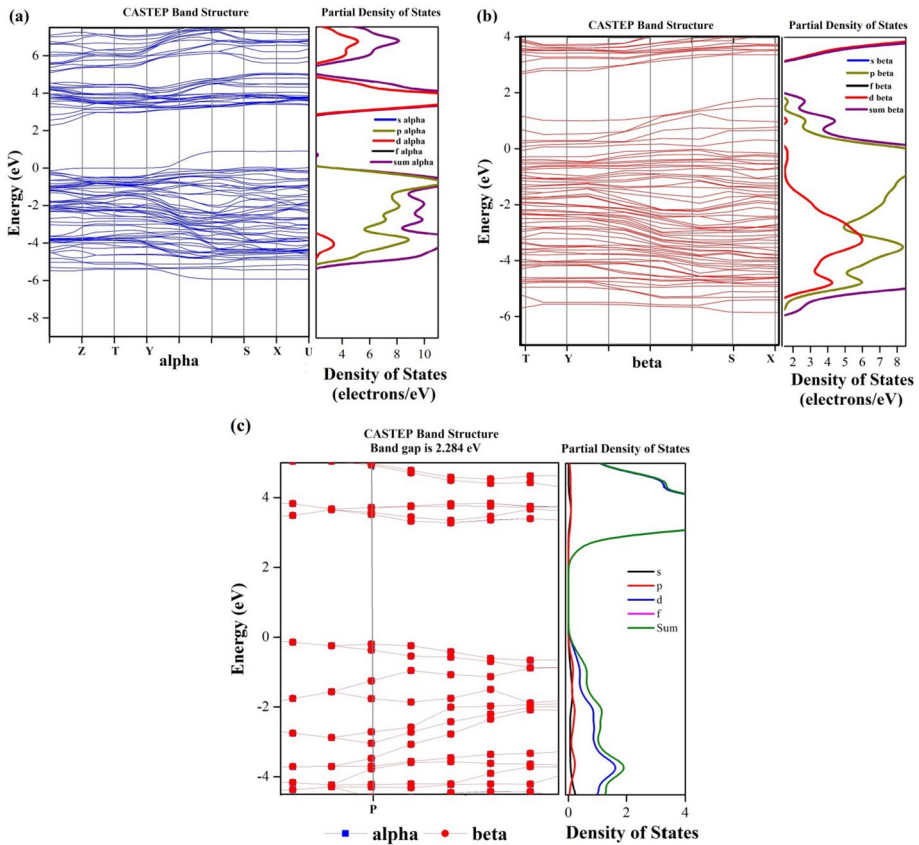


Fig. 20 $\text{Ti}_{1-x}\text{Cu}_x\text{O}_2$ band gaps focused graphics of **a** $\text{Ti}_{1-x}\text{Cu}_x\text{O}_2$ (15:1) band gap, and **b** $\text{Ti}_{1-x}\text{Cu}_x\text{O}_2$ (7.5:1) band gap, **c** stoichiometric TiO_2 band gap

5 Conclusion

$\text{TiO}_2:\text{Cu}_2\text{O}$ nanocomposites were chemically synthesized using two different reducing agents ascorbic acid and sodium boron hydride via hydrothermal method. These chemically synthesized $\text{TiO}_2:\text{Cu}_2\text{O}$ nanocomposites were then used as interlayers via ultrasonic spray pyrolysis to obtain Schottky-type photodiode devices. $I-V$ and $I-t$ measurements were performed to calculate the diode and photodetector parameters.

As can be seen from the results, although it has the same molecular structure and the production processes are the same, the change in the reducing agent in the production method can change the electronic properties. It can be attributed to average particle diameter differences changing from 29 to 38 nm.

Both devices have shown significant responsivity and detectivity. However, the D2 device has shown better photodetector properties compared to the D1. D1 has shown 1.94×10^{10} Jones detectivity and 0.128 A/W responsivity at 80 mW and 100 mW light powers, respectively. D2 has shown 1.07×10^{10} Jones detectivity and 0.264 A/W responsivity at 100 mW light power. The photosensitivity of the device has linear increasing profile with increasing light power. It is noteworthy that both devices demonstrated well-rectifying behaviors as a

result of having low reverse bias and greater forward bias currents at the I – V characteristics in low light. According to the results of our DFT calculations, the band gap narrowed with the addition of Cu_2O which improves the optoelectronic properties. In conclusion, the overall results show that both devices can be utilized in optoelectronic applications.

Author contributions MY: Writing—review and editing, Writing—original draft, Visualization, Validation, Supervision, Methodology, Investigation, Formal analysis, Data curation. SA: Writing—review and editing, Writing—original draft, Visualization, Validation, Investigation, Formal analysis. AAH: Writing—review and editing, Writing—original draft, Visualization, Validation, Investigation, Formal analysis. MOE: Investigation, Formal analysis. OT: Writing—review and editing, Writing—original draft, Supervision. RG: Investigation, Formal analysis. ŞS: Supervision, Data curation, Writing—review and editing, Writing—original draft.

Funding Open access funding provided by the Scientific and Technological Research Council of Türkiye (TÜBİTAK). This work is supported by Selçuk University BAP office with Project Numbers 16401044 and 18701082. Authors would like to acknowledge the support of the Selçuk University for this research. In addition, the study was carried out with the support of TUBITAK (The Scientific and Technological Research Council of Turkey) under Project Number 122Z293.

Data availability statement Data generated and analysed during the current study are available from the corresponding author on reasonable request.

Declarations

Conflict of interest The authors declare that they have no conflict of interest.

Open Access This article is licensed under a Creative Commons Attribution 4.0 International License, which permits use, sharing, adaptation, distribution and reproduction in any medium or format, as long as you give appropriate credit to the original author(s) and the source, provide a link to the Creative Commons licence, and indicate if changes were made. The images or other third party material in this article are included in the article's Creative Commons licence, unless indicated otherwise in a credit line to the material. If material is not included in the article's Creative Commons licence and your intended use is not permitted by statutory regulation or exceeds the permitted use, you will need to obtain permission directly from the copyright holder. To view a copy of this licence, visit <http://creativecommons.org/licenses/by/4.0/>.

References

- Al-Ahmadi, N.A.: Metal oxide semiconductor-based Schottky diodes: a review of recent advances. *Mater. Res. Express* (2020). <https://doi.org/10.1088/2053-1591/ab7a60>
- Anthopoulos, T.D., Singh, B., Marjanovic, N., Sariciftci, N.S., Motta, R., Montaigne Ramil, A., Sitter, H., Cölle, M., de Leeuw, D.M.: High performance n-channel organic field-effect transistors and ring oscillators based on C60 fullerene films. *Appl. Phys. Lett.* **89**, 213504 (2006). <https://doi.org/10.1063/1.2387892>
- Bai, Z., Zhang, Y.: Self-powered UV–visible photodetectors based on $\text{ZnO}/\text{Cu}_2\text{O}$ nanowire/electrolyte heterojunctions. *J. Alloys Compd.* **675**, 325–330 (2016). <https://doi.org/10.1016/j.jallcom.2016.03.051>
- Barakat, N.A.M., Kanjwal, M.A., Chronakis, I.S., Kim, H.Y.: Influence of temperature on the photodegradation process using Ag-doped TiO_2 nanostructures: negative impact with the nanofibers. *J. Mol. Catal. A Chem.* **366**, 333–340 (2013). <https://doi.org/10.1016/j.molcata.2012.10.012>
- Cheung, S.K., Cheung, N.W.: Extraction of Schottky diode parameters from forward current-voltage characteristics. *Appl. Phys. Lett.* **49**, 85–87 (1986). <https://doi.org/10.1063/1.97359>
- Dayan, O., Gencer Imer, A., Al-Sehemi, A.G., Özdemiir, N., Dere, A., Şerbetçi, Z., Al-Ghamdi, A.A., Yakuphanoglu, F.: Photoresponsivity and photodetectivity properties of copper complex-based photodiode. *J. Mol. Struct.* **1200**, 127062 (2020). <https://doi.org/10.1016/j.molstruc.2019.127062>
- Demircioglu, Ö., Karataş, Ş., Yıldırım, N., Bakkaloglu, Ö.F., Türüt, A.: Temperature dependent current–voltage and capacitance–voltage characteristics of chromium Schottky contacts formed by electrodeposition technique on n-type Si. *J. Alloys Compd.* **509**, 6433–6439 (2011). <https://doi.org/10.1016/j.jallcom.2011.03.082>

- Dette, C., Pérez-Osorio, M.A., Kley, C.S., Punke, P., Patrick, C.E., Jacobson, P., Giustino, F., Jung, S.J., Kern, K.: TiO₂ anatase with a bandgap in the visible region. *Nano Lett.* **14**, 6533–6538 (2014). <https://doi.org/10.1021/nl503131s>
- Di Bartolomeo, A.: Graphene Schottky diodes: an experimental review of the rectifying graphene/semiconductor heterojunction. *Phys. Rep.* **606**, 1–58 (2016). <https://doi.org/10.1016/j.physrep.2015.10.003>
- Gullu, H.H., Yıldız, D.E., Kose, D.A., Yıldırım, M.: Si-based photosensitive diode with novel Zn-doped nicotinate/nicotinamide mixed complex interlayer. *Mater. Sci. Semicond. Process.* **147**, 106750 (2022). <https://doi.org/10.1016/j.mssp.2022.106750>
- Hohenberg, P., Kohn, W.: Inhomogeneous electron gas. *Phys. Rev.* **136**, B864–B871 (1964). <https://doi.org/10.1103/PhysRev.136.B864>
- Jiang, M., Yang, K., Yu, H., Yao, L.: Density functional theory of transition metal oxide (FeO, CuO and MnO) adsorbed on TiO₂ surface. *J. Phys. Chem. Solids* **152**, 109957 (2021). <https://doi.org/10.1016/j.jpcs.2021.109957>
- Jin, W., Zhang, K., Gao, Z., Li, Y., Yao, L., Wang, Y., Dai, L.: CdSe nanowire-based flexible devices: schottky diodes, metal-semiconductor field-effect transistors, and inverters. *ACS Appl. Mater. Interfaces* **7**, 13131–13136 (2015). <https://doi.org/10.1021/acsami.5b02929>
- Karadeniz, S., Yıldız, D.E., Gullu, H.H., Kose, D.A., Hussaini, A.A., Yıldırım, M.: Dark and illuminated electrical characteristics of Schottky device with Zn-complex interface layer. *J. Mater. Sci. Mater. Electron.* **33**, 18039–18053 (2022). <https://doi.org/10.1007/s10854-022-08664-1>
- Karataş, Ş., El-Nasser, H.M., Al-Ghamdi, A.A., Yakuphanoglu, F.: High photoresponsivity Ru-doped ZnO/p-Si heterojunction diodes by the sol–gel method. *Silicon* **10**, 651–658 (2018). <https://doi.org/10.1007/s12633-016-9508-7>
- Kern, W., Puotinen, D.A.: Cleaning solutions based on hydrogen peroxide for use in silicon semiconductor technology. *RCA Rev.* **31**, 187–206 (1970)
- Kocyyigit, A., Karteri, İ., Orak, I., Uruş, S., Çaylar, M.: The structural and electrical characterization of Al/GO-SiO₂/p-Si photodiode. *Phys. E Low-Dimens. Syst. Nanostruct.* **103**, 452–458 (2018). <https://doi.org/10.1016/j.physe.2018.06.006>
- Kocyyigit, A., Hussaini, A.A., Yıldırım, M., Kose, D.A., Yıldız, D.E.: Schottky type photodiodes with organic Co-complex and Cd-complex interlayers. *Appl. Organomet. Chem.* (2022a). <https://doi.org/10.1002/aoc.6879>
- Kocyyigit, A., Yıldırım, M., Kose, D.A., Yıldız, D.E.: Synthesize and characterization of Co-complex as interlayer for Schottky type photodiode. *Polym. Bull.* (2022b). <https://doi.org/10.1007/s00289-021-04021-0>
- Kocyyigit, A., Yıldız, D.E., Hussaini, A.A., Kose, D.A., Yıldırım, M.: Cu and Mn centered nicotinamide/nicotinic acid complexes for interlayer of Schottky photodiode. *Curr. Appl. Phys.* (2022c). <https://doi.org/10.1016/j.cap.2022.11.001>
- Koçyığıt, A., Sarılmaz, A., Öztürk, T., Ozel, F., Yıldırım, M.: A Au/CuNiCoS 4 /p-Si photodiode: electrical and morphological characterization. *Beilstein J. Nanotechnol.* **12**, 984–994 (2021). <https://doi.org/10.3762/bjnano.12.74>
- Könenkamp, R., Word, R.C., Godinez, M.: Ultraviolet electroluminescence from ZnO/polymer heterojunction light-emitting diodes. *Nano Lett.* **5**, 2005–2008 (2005). <https://doi.org/10.1021/nl051501r>
- Kyoung, S., Jung, E.-S., Sung, M.Y.: Post-annealing processes to improve inhomogeneity of Schottky barrier height in Ti/Al 4H-SiC Schottky barrier diode. *Microelectron. Eng.* **154**, 69–73 (2016). <https://doi.org/10.1016/j.mee.2016.01.013>
- Li, P., Shivananju, B.N., Zhang, Y., Li, S., Bao, Q.: High performance photodetector based on 2D CH₃NH₃PbI₃ perovskite nanosheets. *J. Phys. D Appl. Phys.* **50**, 094002 (2017). <https://doi.org/10.1088/1361-6463/aa5623>
- Mekki, A., Dere, A., Mensah-Darkwa, K., Al-Ghamdi, A., Gupta, R.K., Harrabi, K., Farooq, W.A., El-Tantawy, F., Yakuphanoglu, F.: Graphene controlled organic photodetectors. *Synth. Met.* **217**, 43–56 (2016). <https://doi.org/10.1016/j.synthmet.2016.03.015>
- Munikrishana Reddy, Y., Nagaraj, M.K., Siva Pratap Reddy, M., Lee, J.-H., Rajagopal Reddy, V.: Temperature-dependent current–voltage (I–V) and capacitance–voltage (C–V) characteristics of Ni/Cu/n-InP schottky barrier diodes. *Braz. J. Phys.* **43**, 13–21 (2013). <https://doi.org/10.1007/s13538-013-0120-7>
- Norde, H.: A modified forward I–V plot for Schottky diodes with high series resistance. *J. Appl. Phys.* **50**, 5052–5053 (1979). <https://doi.org/10.1063/1.325607>
- Nyberg, T.: An alternative method to build organic photodiodes. *Synth. Met.* **140**, 281–286 (2004). [https://doi.org/10.1016/S0379-6779\(03\)00375-8](https://doi.org/10.1016/S0379-6779(03)00375-8)
- Orak, I., Kocyyigit, A., Turut, A.: The surface morphology properties and respond illumination impact of ZnO/n-Si photodiode by prepared atomic layer deposition technique. *J. Alloys Compd.* **691**, 873–879 (2017). <https://doi.org/10.1016/j.jallcom.2016.08.295>

- Perdew, J.P., Burke, K., Ernzerhof, M.: Generalized gradient approximation made simple. *Phys. Rev. Lett.* **77**, 3865–3868 (1996). <https://doi.org/10.1103/PhysRevLett.77.3865>
- Shinen, M.H., AlSaati, S.A.A., Razooqi, F.Z.: Preparation of high transmittance TiO₂ thin films by sol–gel technique as antireflection coating. *J. Phys. Conf. Ser.* **1032**, 012018 (2018). <https://doi.org/10.1088/1742-6596/1032/1/012018>
- Watahiki, T., Yuda, Y., Furukawa, A., Yamamuka, M., Takiguchi, Y., Miyajima, S.: Heterojunction p-Cu₂O/n-Ga₂O₃ diode with high breakdown voltage. *Appl. Phys. Lett.* **111**, 222104 (2017). <https://doi.org/10.1063/1.4998311>
- Wei, H.M., Gong, H.B., Chen, L., Zi, M., Cao, B.Q.: Photovoltaic efficiency enhancement of Cu₂O solar cells achieved by controlling homojunction orientation and surface microstructure. *J. Phys. Chem. C* **116**, 10510–10515 (2012). <https://doi.org/10.1021/jp301904s>
- Wis, G., Sawicka-Chudy, P., Wal, A., Sibiński, M., Potera, P., Yavorskyi, R., Nykyryu, L., Ploch, D., Bester, M., Cholewa, M., Chernikova, O.M.: Structure defects and photovoltaic properties of TiO₂:ZnO/CuO solar cells prepared by reactive DC magnetron sputtering. *Appl. Sci.* **13**, 3613 (2023). <https://doi.org/10.3390/app13063613>
- Yakuphanoglu, F.: Electrical characterization and interface state density properties of the ITO/C 70/Au Schottky diode. *J. Phys. Chem. C* **111**, 1505–1507 (2007a). <https://doi.org/10.1021/jp066912q>
- Yakuphanoglu, F.: Photovoltaic properties of hybrid organic/inorganic semiconductor photodiode. *Synth. Met.* **157**, 859–862 (2007b). <https://doi.org/10.1016/j.synthmet.2007.08.012>
- Yao, Z.Q., Liu, S.L., Zhang, L., He, B., Kumar, A., Jiang, X., Zhang, W.J., Shao, G.: Room temperature fabrication of p-channel Cu₂O thin-film transistors on flexible polyethylene terephthalate substrates. *Appl. Phys. Lett.* **101**, 042114 (2012). <https://doi.org/10.1063/1.4739524>
- Yathisha, R.O., Arthoba Nayaka, Y.: Structural, optical and electrical properties of zinc incorporated copper oxide nanoparticles: doping effect of Zn. *J. Mater. Sci.* **53**, 678–691 (2018). <https://doi.org/10.1007/s10853-017-1496-5>
- Yathisha, R.O., Nayaka, Y.A.: Effect of solvents on structural, optical and electrical properties of ZnO nanoparticles synthesized by microwave heating route. *Inorg. Chem. Commun.* **115**, 107877 (2020). <https://doi.org/10.1016/j.inoche.2020.107877>
- Yathisha, R.O., Nayaka, Y.A., Vidyasagar, C.C.: Microwave combustion synthesis of hexagonal prism shaped ZnO nanoparticles and effect of Cr on structural, optical and electrical properties of ZnO nanoparticles. *Mater. Chem. Phys.* **181**, 167–175 (2016). <https://doi.org/10.1016/j.matchemphys.2016.06.046>
- Yathisha, R.O., Arthoba Nayaka, Y., Manjunatha, P., Purushothama, H.T., Vinay, M.M., Basavarajappa, K.V.: Study on the effect of Zn²⁺ doping on optical and electrical properties of CuO nanoparticles. *Phys. E Low-Dimens. Syst. Nanostruct.* **108**, 257–268 (2019a). <https://doi.org/10.1016/j.physe.2018.12.021>
- Yathisha, R.O., Arthoba Nayaka, Y., Manjunatha, P., Vinay, M.M., Purushothama, H.T.: Doping, structural, optical and electrical properties of Ni²⁺ doped CdO nanoparticles prepared by microwave combustion route. *Microchem. J.* **145**, 630–641 (2019b). <https://doi.org/10.1016/j.microc.2018.10.060>
- Yenel, E., Torlak, Y., Kocyigit, A., Erden, İ, Kuş, M., Yıldırım, M.: W- and Mo-based polyoxometalates (POM) as interlayer in Al/n-Si photodiodes. *J. Mater. Sci. Mater. Electron.* **32**, 12094–12110 (2021). <https://doi.org/10.1007/s10854-021-05838-1>
- Yıldırım, M.: Determination of contact parameters of Au/n-Ge Schottky barrier diode with rubrene interlayer. *Politekn. Derg.* **20**, 165–173 (2017)
- Yıldırım, M., Kocyigit, A.: Characterization of Al/In:ZnO/p-Si photodiodes for various In doped level to ZnO interfacial layers. *J. Alloys Compd.* **768**, 1064–1075 (2018). <https://doi.org/10.1016/j.jallcom.2018.07.295>
- Yıldırım, M., Kocyigit, A., Sarılmaz, A., Ozel, F.: The effect of the triangular and spherical shaped CuSbS₂ structure on the electrical properties of Au/CuSbS₂/p-Si photodiode. *J. Mater. Sci. Mater. Electron.* **30**, 332–339 (2019). <https://doi.org/10.1007/s10854-018-0297-1>
- Yıldırım, M., Kocyigit, A., Torlak, Y., Yenel, E., Hussaini, A.A., Kuş, M.: Electrical behaviors of the Co- and Ni-based POMs interlayered Schottky photodetector devices. *Adv. Mater. Interfaces* (2022). <https://doi.org/10.1002/admi.202102304>
- Yılmaz, M., Caldiran, Z., Deniz, A.R., Aydoğan, S., Gunturkun, R., Turut, A.: Preparation and characterization of sol–gel-derived n-ZnO thin film for Schottky diode application. *Appl. Phys. A* **119**, 547–552 (2015). <https://doi.org/10.1007/s00339-015-8987-5>
- Yılmaz, M., Kocyigit, A., Cirak, B.B., Kacus, H., Incekara, U., Aydoğan, S.: The comparison of Co/hematoxylin/n-Si and Co/hematoxylin/p-Si devices as rectifier for a wide range temperature. *Mater. Sci. Semicond. Process.* **113**, 105039 (2020). <https://doi.org/10.1016/j.mssp.2020.105039>
- Yücedağ, İ, Kaya, A., Altındal, Ş, Uslu, İ: Electrical and dielectric properties and intersection behavior of G/ω-V plots for Al/Co-PVA/p-Si (MPS) structures at temperatures below room temperature. *J. Korean Phys. Soc.* **65**, 2082–2089 (2014). <https://doi.org/10.3938/jkps.65.2082>

Zang, Z.: Efficiency enhancement of ZnO/Cu₂O solar cells with well oriented and micrometer grain sized Cu₂O films. *Appl. Phys. Lett.* **112**, 042106 (2018). <https://doi.org/10.1063/1.5017002>

Publisher's Note Springer Nature remains neutral with regard to jurisdictional claims in published maps and institutional affiliations.

Authors and Affiliations

Sinem Aksan¹ · **Ali Akbar Hussaini**^{2,3} · **Mehmet Okan Erdal**⁴ · **Oğuzhan Taştan**⁵ · **Rabia Güzel**⁵ · **Şerife Saçmacı**^{5,6} · **Murat Yıldırım**²

✉ Sinem Aksan
sinem.aksan@dpu.edu.tr

✉ Şerife Saçmacı
sacmaci@erciyes.edu.tr

✉ Murat Yıldırım
muratyildirim@selcuk.edu.tr

¹ Department of Metallurgy and Materials Engineering, Faculty of Engineering, Kutahya Dumlupınar University, 43100 Kutahya, Turkey

² Department of Biotechnology, Faculty of Science, Selcuk University, 42130 Konya, Turkey

³ Faculty of Biotechnology and Food Science, Wrocław University of Environmental and Life Sciences, 51630 wrocław, Poland

⁴ Meram Vocational School, Necmettin Erbakan University, 42090 Konya, Turkey

⁵ Nanotechnology Research Center, Erciyes University, 38039 Kayseri, Turkey

⁶ Department of Chemistry, Faculty of Sciences, Erciyes University, 38039 Kayseri, Turkey